Ultrabroadband single-cycle terahertz pulses with peak fields of 300 kV cm^{-1} from a metallic spintronic emitter

T. Seifert[1], S. Jaiswal[2,3], M. Sajadi[1], G. Jakob[2], S. Winnerl[4], M. Wolf[1], M. Kläui[2], T. Kampfrath[1,*]

1. Department of Physical Chemistry, Fritz Haber Institute of the Max Planck Society, 14195 Berlin, Germany
2. Institute of Physics, Johannes Gutenberg University Mainz, 55099 Mainz, Germany
3. Singulus Technologies AG, 63796 Kahl am Main, Germany
4. Helmholtz-Zentrum Dresden-Rossendorf, 01328 Dresden, Germany

[*] E-mail: kampfrath@fhi-berlin.mpg.de

We explore the capabilities of metallic spintronic thin-film stacks as a source of intense and broadband terahertz electromagnetic fields. For this purpose, we excite a W/CoFeB/Pt trilayer (thickness of 5.6 nm) on a large-area glass substrate (diameter of 7.5 cm) by a femtosecond laser pulse (energy 5.5 mJ, duration 40 fs, wavelength 800 nm). After focusing, the emitted terahertz pulse is measured to have a duration of 230 fs, a peak field of 300 kV cm^{-1} and an energy of 5 nJ. In particular, the waveform exhibits a gapless spectrum extending from 1 to 10 THz at 10% of its amplitude maximum, thereby facilitating nonlinear control over matter in this difficult-to-reach frequency range on the sub-picosecond time scale.

Terahertz (THz) pulses covering the range from 1 to 20 THz are resonant probes of numerous low-energy excitations in all phases of matter. Completely unexplored research avenues open up when THz pulses are used to drive rather than probe material resonances.[1,2,3,4,5,6] In solids, examples are the ultrafast coherent control over the motion of lattice ions and ordered electron spins, and the transport of charge carriers, even across the atomic-scale junction of scanning tunneling microscopes.[7] To implement such material control, elevated field strengths >100 kV cm^{-1} over a wide frequency range are required. Furthermore, to access more resonances with better time resolution, higher bandwidth is highly desirable.

User facilities based on electron accelerators can provide both broadband and narrowband THz pulses with tunable center frequency, peak fields approaching 1 MV cm^{-1} and repetition rates as high as 1 MHz.[8] Table-top sources,[9] on the other hand, operate at a rate of typically ~1 kHz. They are based on optical rectification in photoconductive switches,[10] inorganic[11] and organic[12,13,14] crystals at the low-frequency side. For frequencies above 5 THz, difference frequency mixing of the two outputs of a dual optical parametric amplifier[15,16] was shown to yield field strengths >100 MV cm^{-1}.[15] Regardless of the high conversion efficiencies reached with these schemes, they are affected by spectral gaps between 1 and 10 THz. Emission from a dual-color-laser-excited air plasma[17] can even cover frequencies from below 1 to above 10 THz with field strengths of up to 8 MV cm^{-1}.[18] However, the experimental realization is not as straightforward as with emitters relying on optical rectification. Thus, the frequency range from about 5 to 15 THz is still challenging in terms of high fields and table-top setups.[19]

Recently, metallic[20,21] and metallic spintronic[22,23,24,25,26] heterostructures were shown to be promising THz emitters. In particular, when a W/CoFeB/Pt trilayer of 5.6 nm thickness was excited with 10 fs, ~1 nJ optical pulses from an 80 MHz laser oscillator, THz pulses with a gapless spectrum from 1 to 30 THz and a conversion efficiency even better than standard oscillator-based THz sources were achieved.[27] However, the capability of spintronic THz emitters as high-field sources driven by millijoule-class laser pulses remains to be shown.

Here, we demonstrate upscaling of metallic spintronic THz emitters, resulting in a practical and ultrabroadband source delivering THz pulses as short as 230 fs, a spectrum from 1 to 10 THz (full width at 10% of amplitude maximum) and peak fields of 300 kV cm^{-1}.

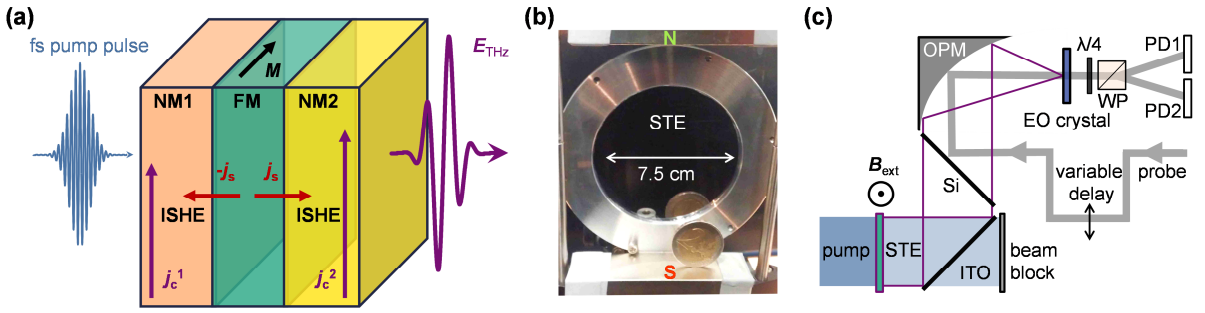

FIG. 1. High-field spintronic terahertz emitter (STE). (a) Principle of operation. A femtosecond laser pulse drives spin currents $\boldsymbol{j_s}$ from a ferromagnetic (FM) layer (with in-plane magnetization $\boldsymbol{M}$) into two adjacent non-magnetic (NM) layers. The inverse spin Hall effect (ISHE) converts these spin currents into orthogonal in-plane charge currents $\boldsymbol{j_c^1}$ and $\boldsymbol{j_c^2}$. By design, NM1 and NM2 have opposite spin Hall angles, thereby resulting in constructive superposition of the two sub-picosecond charge currents. Consequently, a THz pulse $\boldsymbol{E_{THz}}$ is emitted into the optical far-field. (b) Photograph of the spintronic terahertz emitter. Two bar magnets labeled N and S provide a magnetic field of ≥10 mT across the entire emitter area. A 2 € coin serves as a scale reference. (c) Schematic of the experimental setup. For details, see the main text. Abbreviations: $\boldsymbol{B_{ext}}$: external magnetic field, ITO: indium-tin-oxide-covered glass, Si: silicon wafer, OPM: off-axis parabolic mirror, EO: electrooptic, λ/4: quarter-wave plate, WP: Wollaston prism, PD: photodiode.

Our metallic spintronic THz emitter[27] [STE, see Figs. 1(a) and 1(b)] is a nanometer-thick trilayer structure NM1/FM/NM2, made of a ferromagnetic (FM) layer FM=$Co_{20}Fe_{60}B_{20}$ between two non-magnetic (NM) layers NM1=Pt and NM2=W on a fused-silica substrate, which also acts as a heat sink. The detailed stack structure is fused silica (thickness of 500 µm) | W (1.8 nm) | $Co_{20}Fe_{60}B_{20}$ (2 nm) | Pt (1.8 nm) (see Supplementary Material). The cost of the emitter is mainly determined by the substrate price of ~$20 for 7.5 cm diameter.

Upon excitation with a near-infrared femtosecond pump pulse, a distribution of non-equilibrium electrons is created in the emitter. Importantly, the transport properties of the majority- and minority-spin electrons in the FM layer (i.e. lifetimes, densities and group velocities) differ distinctly. Consequently, and in analogy to the spin-dependent Seebeck effect (SDSE)[28], spin currents polarized parallel to the sample magnetization are injected from the FM into the adjacent NM layers where spin-orbit coupling causes a spin-dependent deflection of the electrons. This inverse spin Hall effect (ISHE) transforms the spin current into a sub-picosecond transverse charge-current burst[29] that emits a THz electromagnetic pulse. NM materials showing a particularly large ISHE, yet with opposite sign of the spin Hall angle, are Pt and W.

In our experiment [see Fig. 1(c) for a schematic], we use laser pulses (energy of 5.5 mJ, center wavelength of 800 nm, duration of 40 fs, repetition rate of 1 kHz) from an amplified Ti:sapphire laser system (Coherent Legend Elite Duo). The collimated beam [diameter of 4.8 cm full width at half maximum (FWHM) of intensity] is incident onto the STE, whose in-plane magnetization is saturated by permanent magnets delivering a field of about ±10 mT. To spectrally separate the pump from the THz radiation, the emitted THz beam is reflected by a float glass with indium-tin-oxide coating (thickness of 100 nm, sheet resistance <7 Ω/sq, covered with a SiO_2 passivation layer) under an angle of 45°. After transmission through a silicon wafer (angle of incidence of 45°±2°), blocking the residual pump radiation, the THz beam is eventually focused on two different detectors to characterize the THz power and the transient THz electric field. The THz power is measured with a power meter (Gentec THz-B), which requires chopping of the near-infrared pump beam at 25 Hz. To determine the THz polarization state, we employ a rotatable free-standing wire-grid polarizer (InfraSpecs model P02) placed directly behind the silicon wafer.

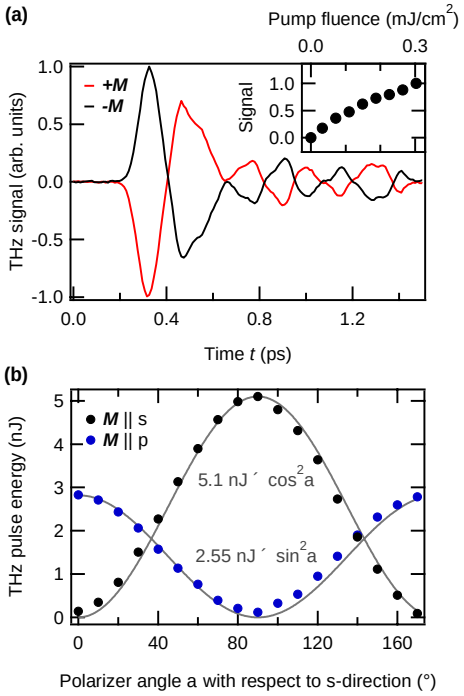

FIG. 2. Raw data. (a) Typical THz electrooptic signals measured with a 50 µm thick Quartz detector for opposite sample magnetizations $\pm \boldsymbol{M}$. The inset shows the pump-fluence dependence of the THz signal (root mean square). (b) THz pulse energy as a function of the rotation angle $\boldsymbol{\alpha}$ of a THz polarizer inserted before the THz power meter for two orthogonal sample magnetizations (black and blue dots). Grey lines are $\mathbf{cos^2}\,\boldsymbol{\alpha}$ and $\mathbf{sin^2}\,\boldsymbol{\alpha}$ fits. THz pulse energies are corrected for polarizer transmission losses.

We characterize the transient THz electric field by standard electrooptic (EO) sampling using a femtosecond probe pulse from the seed oscillator (energy of 0.6 nJ, center wavelength of 750 nm, duration of 8 fs, repetition rate of 80 MHz) that is coupled into the THz beam path upon reflection from the rear side of the silicon wafer [Fig. 1(c)]. Both beams are focused by a 45° off-axis parabolic mirror (focal length of 2") into the EO detection crystal of either (110)-oriented GaP (thickness of 50 µm), (110)-oriented ZnTe (10 and 50 µm) or (001)-oriented Quartz (50 µm). The THz-field-induced probe ellipticity is measured by an optical bridge [Fig. 1(c)]. The detection crystals are sufficiently thin to ensure a linear scaling of the EO signal with the THz electric field. If not mentioned otherwise, measurements are conducted at room temperature in air. Details on EO detection with a Quartz crystal will be published elsewhere.

Figure 2(a) shows a typical EO signal as recorded with a 50 µm thick Quartz crystal. We observe an almost complete reversal of the THz signal when the sample magnetization is reversed. This behavior is consistent with our understanding of the THz emission process [see above, Fig. 1(a) and Ref. 27]. The pump-fluence dependence [inset of Fig. 2(a)] demonstrates that the THz emission is still well below saturation. We note that the temporal shape of the THz pulse is independent of the pump fluence (not shown). The observed ringing after the main pulse [Fig. 2(a)] may arise from the THz absorption of water vapor in air. This notion is corroborated by the fact that additional purging with N_2 leads to a 10% increase in THz amplitude and a slight reduction of the ringing. Another possible origin is the absorption by phonon resonances of the EO Quartz detector at around 4, 8 and 12 THz.[30,31]

Figure 2(b) displays the measured THz power behind a wire-grid polarizer as a function of its azimuthal rotation angle α for the sample magnetization set perpendicular ($\boldsymbol{M} \parallel \mathrm{s}$) and parallel ($\boldsymbol{M} \parallel \mathrm{p}$) to the optical table. The measured data are well described by an α-dependence following $\cos^2 \alpha$ and $\sin^2 \alpha$. Therefore, the THz radiation measured by the power detector is polarized linearly and oriented perpendicularly to the sample magnetization. These polarization properties agree with the SDSE/ISHE THz emission scenario of Fig. 1(a). The different maximum power amplitudes obtained for the $\boldsymbol{M} \parallel \mathrm{s}$- and $\boldsymbol{M} \parallel \mathrm{p}$-configurations can easily be explained by the polarization-dependent transmittance of the silicon window [see Fig. 1(c)]: a calculation of the Fresnel transmission coefficients yields a transmittance ratio of p- and s-polarized THz radiation of 2.0 ± 0.1 (Ref. 32). This value is in good agreement with the experimental observation [see Fig. 2(b)]. By accounting for the transmittance of the polarizer (86%, averaged over the THz intensity spectrum[33]), we obtain an energy of about 5.1 nJ for a p-polarized THz pulse.

We note that both coherent THz pulses and incoherent black-body radiation of the

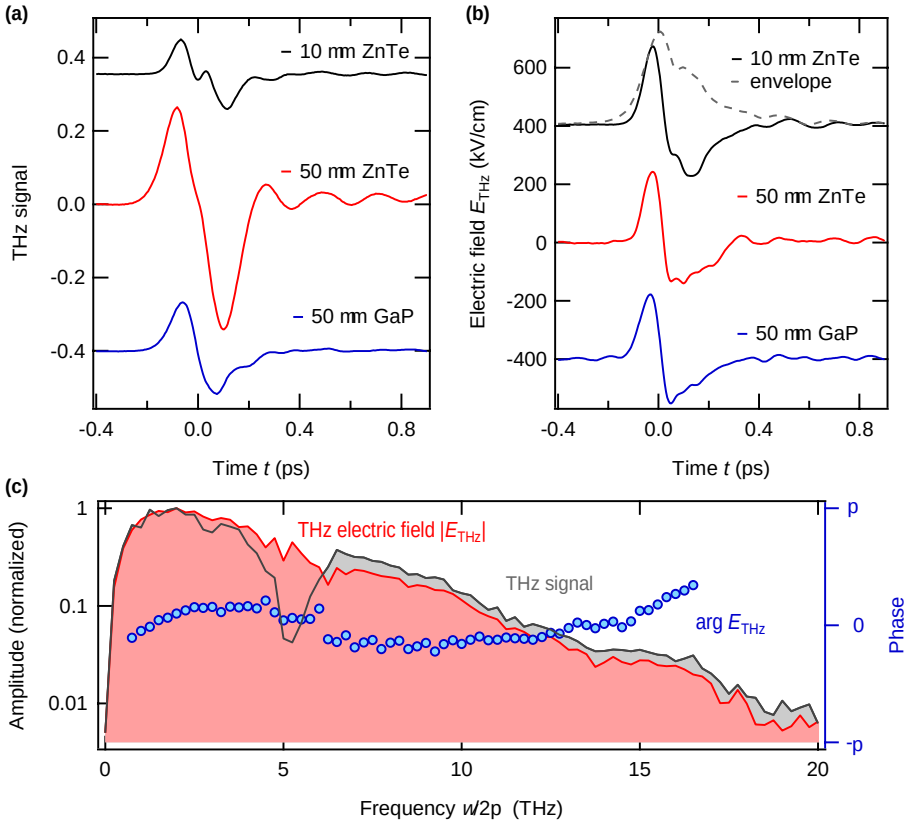

FIG. 3. THz-electric-field extraction. (a) Electrooptic signals as recorded with three different detection crystals (10 µm ZnTe, 50 µm ZnTe and 50 µm GaP) in a dry nitrogen atmosphere. (b) Resulting THz electric fields at the detector position obtained by deconvolution of the detector response function. The grey dashed line is the field envelope. Curves in panels (a) and (b) are offset for clarity. (c) Spectra of signal amplitude, electric-field amplitude and field phase as obtained with the 10 µm thick ZnTe detector.

pump-heated STE can contribute to the measured THz power. In addition, THz radiation can also be generated by the residual pump light absorbed in the silicon beam combiner [Fig. 1(c)]. However, the coherent part of the THz emission from the silicon slab is expected to be independent of the STE's magnetization direction, in contrast to the measurements of Fig. 2(a). Similarly, the black-body radiation from both STE and silicon slab is largely unaffected by the external magnetic field. Therefore, the power behind the polarizer should be identical for the $\boldsymbol{M} \parallel$ p - and $\boldsymbol{M} \parallel$ s -configurations, in stark contrast to our observations [see Fig. 2(b)]. Thus, the black-body radiation arriving at the power detector makes a minor or even negligible contribution to the detector signal. This observation can be explained by the following two scenarios.

First, the black-body radiation arriving at the detector has a much smaller power than the coherent THz radiation. Second, the instantaneous temperature of STE and silicon wafer and the resulting black-body radiation are not able to follow the pump-power modulation frequency of 25 Hz, thereby being suppressed by our phase-locked power detector. Therefore, each coherent THz pulse stems from the STE and has an energy of 5.1 nJ and a linear polarization perpendicular to the sample magnetization.

To extract the actual THz electric field at the detector position, the measured EO signal is deconvoluted with respect to the transfer function of the EO detection process.[34,35] The deconvolution is performed in the time domain for three different detector crystals [10 µm thick ZnTe on a (100)-oriented ZnTe substrate[34], 50 µm thick free-standing ZnTe and GaP]. The resulting field waveforms are low-pass filtered

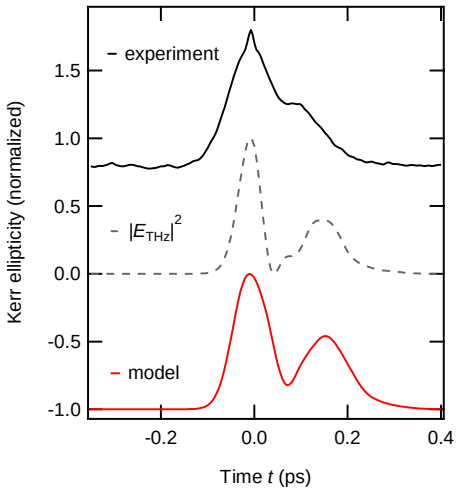

FIG. 4. THz Kerr effect of diamond. Transient ellipticity (solid black) of a near-infrared probe pulse induced by a THz pump pulse generated with our STE. The squared THz electric field (dashed grey) and the simulated Kerr ellipticity (solid red) are also shown. For details of the model, see the main text. All curves are normalized to 1 and offset for clarity.

with a Gaussian function centered at 0 THz and having a FWHM of 40 THz.

Figure 3(a) shows typical EO signals recorded in a dry nitrogen atmosphere with the three different detectors. The signal strength equals twice the ellipticity acquired by the probe pulse. The extracted THz electric fields $E_{\mathrm{THz}}(t)$ are displayed in Fig. 3(b).

We find single-cycle waveforms whose temporal shape and amplitude are in excellent agreement for all detectors used. This observation demonstrates the robustness of our deconvolution scheme. The extracted transient THz electric field reaches a peak value of 300 kV cm^{-1} and has a duration of 230 fs [FWHM of the field envelope, see Fig. 3(b)]. Fourier-transformation of the field waveforms $E_{\mathrm{THz}}(t)$ yields the complex-valued field amplitude spectrum $|E_{\mathrm{THz}}(\omega)|$ vs frequency $\omega/2\pi$ that is shown in Fig. 3(c) along with the respective THz signal spectrum. Note that the THz field spectrum is gapless and spans the entire range from 0.1 to 10 THz with respect to 10% of the peak spectral amplitude. The spectral phase is flat and varies by less than $2\pi/10$ (standard deviation).

As a cross-check, we compare the extracted transient THz electric field $E_{\mathrm{THz}}(t)$ in the focus [Fig. 3(b)] to the measured THz pulse energy W [Fig. 2(b)], which are related by

$$W = C \int_{-\infty}^{\infty} \mathrm{d}\omega \; |E_{\mathrm{THz}}(\omega)|^2/\omega^2. \qquad (1)$$

Here, $C = 2\pi \ln 2\, c^2 f^2/Z_0 b^2$, c is the vacuum speed of light, $Z_0 \approx 377\,\Omega$ is the free-space impedance, $f = 5.1$ cm is the focal length of the parabolic mirror, and $b = 2.4$ cm is the beam radius at half intensity maximum (see Supplementary Material). Using the measured THz electric field in the focus [Fig. 3(b)] and Eq. (1), we obtain a THz pulse energy of 4.1 nJ, which is in excellent agreement with the directly measured value of 5.1 nJ.

To demonstrate the capability of these pulses for THz nonlinear optics, we measure the THz Kerr effect[36,37,38] of diamond. To study this $\chi^{(3)}$ -type nonlinear optical effect, the p-polarized THz transient is focused into a 320 µm thick polycrystalline diamond crystal in a dry nitrogen atmosphere. We measure the transient birefringence using a co-propagating probe beam with the same pulse specifications as in EO sampling, but linearly polarized with an angle of 45° with respect to the THz electric field direction.

Figure 4 shows the induced ellipticity acquired with a moderate measurement time of 5 min. Its striking similarity to the squared THz electric field suggests the sample response to be quadratic in the THz field, that is, of $\chi^{(3)}$-type. To support this understanding, we simulate the Kerr-type pump-probe signal by taking the velocity mismatch between pump and probe beam into account.[38] As seen in Fig. 4, we find good agreement with the measured data. Small discrepancies may originate from neglecting lensing effects due to the sharply focused THz field[39] and the dispersion of diamond's THz refractive index. The THz Kerr effect observed here demonstrates the capability of the STE as a high-field THz source.

In conclusion, a large-area spintronic emitter of only 5.6 nm thickness is implemented as a high-field THz source. Excitation by 5.5 mJ optical pump pulses results in single-cycle THz pulses with a duration of only 230 fs (FWHM of field amplitude) and peak electric fields of 300 kV cm^{-1}. The capability of these THz pulses in terms of driving non-linear effects is demonstrated by inducing a transient $\chi^{(3)}$-response in diamond. We note that the THz generation mechanism relies on ultrafast electron

heating and should, therefore, be virtually independent of the pump wavelength. The combination of ease-of-use, versatility and scalability makes this high-field emitter concept very interesting for THz nonlinear optics. It holds the promise for an even improved emitter performance in the near future.

We emphasize that this work is only a first step toward spintronic strong-field THz sources. Numerous improvements are anticipated, for example by optimization of the fluence and duration of the pump pulse. Finally, in terms of the emitter itself, many degrees of freedom can be tuned, including the emitter temperature, the choice of materials with large spin Hall angle[40], the layer sequence and the arrangement of cascaded emitters.[41]

Supplementary material

See Supplementary Material for details on the sample preparation and on the calculation of the pulse energy.

Acknowledgments

T.S., M.S., M.W. and T.K. acknowledge the European Research Council for funding through the ERC H2020 CoG project TERAMAG/Grant No. 681917 and the German Research Foundation for funding through Grant No. KA 3305/2-1 of the priority program SPP 1538/SpinCaT. S.J., G.J., and M.K. acknowledge funding by the European Community under the Marie-Curie FP7 program, ITN "WALL" (Grant No. 608031), the German Research Foundation (in particular SFB TRR173/Spin+X) and the Graduate School of Excellence Materials Science in Mainz (MAINZ, GSC 266).

[1] M. C. Hoffmann, Terahertz Spectroscopy and Imaging (Springer Berlin, Heidelberg, 2012) pp. 355-388.
[2] T. Kampfrath, K. Tanaka, and K. A. Nelson, Nat. Photon. **7**, 680-690 (2013).
[3] H. Y. Hwang, S. Fleischer, N. C. Brandt, B. G. Perkins Jr, M. Liu, K. Fan, A. Sternbach, X. Zhang, R. D. Averitt, and K. A. Nelson, J. Mod. Opt. **62**, 1447-1479 (2015).
[4] T. Elsaesser, K. Reimann, and M. Woerner, J. Chem. Phys. **142**, 212301 (2015).
[5] D. Nicoletti, and A. Cavalleri, Adv. Opt. Photon. **8**, 401-464 (2016).
[6] S. D. Ganichev, and W. Prettl, Intense Terahertz Excitation of Semiconductors (Oxford University Press, Oxford, 2006) pp. 1-380.
[7] T. L. Cocker, D. Peller, P. Yu, J. Repp, and R. Huber, Nature **539**, 263-267 (2016).
[8] B. Green, S. Kovalev, V. Asgekar, G. Geloni, Lehnert, T. Golz, M. Kuntzsch, C. Bauer, J. Hauser, J. Voigtlaender, B. Wustmann, I. Koesterke, M. Schwarz, M. Freitag, A. Arnold, J. Teichert, M. Justus, W. Seidel, C. Ilgner, N. Awari, D. Nicoletti, S. Kaiser, Y. Laplace, S. Rajasekaran, L. Zhang, S. Winnerl, H. Schneider, G. Schay, I. Lorincz, A. A. Rauscher, I. Radu, S. Mährlein, T. H. Kim, J. S. Lee, T. Kampfrath, S. Wall, J. Heberle, A. Malnasi-Csizmadia, A. Steiger, A. S. Müller, M. Helm, U. Schramm, T. Cowan, P. Michel, A. Cavalleri, A. S. Fisher, N. Stojanovic, and M. Gensch, Sci. Rep. **6**, 22256 (2016).
[9] X. C. Zhang, A. Shkurinov, and Y. Zhang, Nat. Photon. **11**, 16-18 (2017).
[10] C.W. Berry, N. Wang, M.R. Hashemi, M. Unlu, and M. Jarrahi, Nat. Commun. **4**, 1622 (2013).
[11] J. A. Fülöp, G. Polónyi, B. Monoszlai, G. Andriukaitis, T. Balciunas, A. Pugzlys, G. Arthur, A. Baltuska, and J. Hebling, Optica **3**, 1075-1078 (2016).
[12] H. Hirori, A. Doi, F. Blanchard, and K. Tanaka, Appl. Phys. Lett. **98**, 091106 (2011).
[13] C. P. Hauri, C. Ruchert, C. Vicario, and F. Ardana, Appl. Phys. Lett. **99**, 161116 (2011).
[14] C. Vicario, M. Jazbinsek, A. V. Ovchinnikov, O. V. Chefonov, S. I. Ashitkov, M. B. Agranat, and C. P. Hauri, Opt. Express **23**, 4573-4580 (2015).
[15] A. Sell, A. Leitenstorfer, and R. Huber, Opt. Lett. **33**, 2767-2769 (2008).
[16] B. Liu, H. Bromberger, A. Cartella, T. Gebert, M. Först, and A. Cavalleri, Opt. Lett. 42, 129-131 (2017).
[17] K. Kim, J. Glownia, A. J. Taylor, and G. Rodriguez, IEEE J. Quantum Electron. **48**, 797-805 (2012).
[18] T. I. Oh, Y. J. Yoo, Y. S. You, and K. Y. Kim, Appl. Phys. Lett. **105**, 041103 (2014).
[19] S. S. Dhillon, M. S. Vitiello, E. H. Linfield, A. G. Davies, M. C. Hoffmann, J. Booske, C. Paoloni, M. Gensch, P. Weightman, G. P. Williams, E. Castro-Camus, D. R. S. Cumming, F. Simoens, I. Escorcia-Carranza, .J Grant, S. Lucyszyn, M. Kuwata-Gonokami, K. Konishi, M. Koch, C. A. Schmuttenmaer, T. L. Cocker, R. Huber, A. G. Markelz, Z. D. Taylor, V. P. Wallace, J. A. Zeitler, J. Sibik, T. M. Korter, B. Ellison, S. Rea, P. Goldsmith, K. B. Cooper, R. Appleby, D. Pardo, P. G. Huggard, V. Krozer, H. Shams, M. Fice, C. Renaud, A. Seeds,

A. Stöhr, M. Naftaly, N. Ridler, R. Clarke, J. E. Cunningham, and M. B. Johnston, J. Phys. D: Appl. Phys. **50**, 043001 (2017).
[20] G. K. P. Ramanandan, G. Ramakrishnan, N. Kumar, A. J. L. Adam, and P. C. M. Planken, J. Phys. D: Appl. Phys. **47**, 374003 (2014).
[21] D. K. Polyushkin, I. Márton, P. Rácz, P. Dombi, E. Hendry, and W. L. Barnes, Phys. Rev. B **89**, 125426 (2014).
[22] T. Kampfrath, M. Battiato, P. Maldonado, G. Eilers, J. Nötzold, S. Mährlein, V. Zbarsky, F. Freimuth, Y. Mokrousov, S. Blügel, M. Wolf, I. Radu, P. M. Oppeneer, and M. Münzenberg, Nat. Nanotech. **8**, 256-260 (2013).
[23] T. J. Huisman, and T. Rasing, J. Phys. Soc. Jpn. **86**, 011009 (2016).
[24] Y. Wu, M. Elyasi, X. Qiu, M. Chen, Y. Liu, L. Ke, and H. Yang, Adv. Mater. **29**, 1603031 (2017).
[25] D. Yang, J. Liang, C. Zhou, L. Sun, R. Zheng, S. Luo, Y. Wu, and J. Qi, Adv. Opt. Mat. **4**, 1944-1949 (2016).
[26] N. Awari, S. Kovalev, C. Fowley, K. Rode, R. A. Gallardo, Y-C. Lau, D. Betto, N. Thiyagarajah, B. Green, O. Yildirim, J. Lindner, J. Fassbender, J. M. D. Coey, A. M. Deac, and M. Gensch, Appl. Phys. Lett. **109**, 032403 (2016).
[27] T. Seifert, S. Jaiswal, U. Martens, J. Hannegan, L. Braun, P. Maldonado, F. Freimuth, A. Kronenberg, J. Henrizi, I. Radu, E. Beaurepaire, Y. Mokrousov, P. M. Oppeneer, M. Jourdan, G. Jakob, D. Turchinovich, L. M. Hayden, M. Wolf, M. Münzenberg, M. Kläui, and T. Kampfrath, Nat. Photon. **10**, 483-488 (2016).
[28] K. Uchida, S. Takahashi, K. Harii, J. Ieda, W. Koshibae, K. Ando, S. Maekawa, and E. Saitoh, Nature **455**, 778-781 (2008).
[29] J. Wunderlich, B. Kaestner, J. Sinova and T. Jungwirth, Phys. Rev. Lett. **94**, 047204 (2005).
[30] E. E. Russell, and E. E. Bell, J. Opt. Soc. Am. **57**, 341-348 (1967).
[31] W. G. Spitzer, and D. A. Kleinman, Phys. Rev. **121**, 1324 (1961).
[32] J. Dai, J. Zhang, W. Zhang, and D. Grischkowsky, J. Opt. Soc. Am. B **21**, 1379-1386 (2004).
[33] See http://www.infraspecs.de/html/ir_polarizer_p02.html for the polarizer transmission function
[34] A. Leitenstorfer, S. Hunsche, J. Shah, M. C. Nuss, and W. H. Knox, Appl. Phys. Lett. **74**, 1516 (1999).
[35] T. Kampfrath, J. Nötzold, and M. Wolf, Appl. Phys. Lett. **90**, 231113 (2007).
[36] M. C. Hoffmann, N. C. Brandt, H. Y. Hwang, K. L. Yeh, and K. A. Nelson, Appl. Phys. Lett. **95**, 231105 (2009).
[37] M. Cornet, J. Degert, E. Abraham, and E. Freysz, J. Opt. Soc. Am. B **31**, 1648-1652 (2014).
[38] M. Sajadi, M. Wolf, and T. Kampfrath, Opt. Express **23**, 28985-28992 (2015).
[39] A. Schneider, Arno, Opt. Lett. **34**, 1054-1056 (2009).
[40] K. Demasius, T. Phung, W. Zhang, B. P. Hughes, S. Yang, A. Kellock, W. Han, A. Pushp, and S. S. P. Parkin, Nat. Commun. **7**, 10644 (2016).
[41] M. Sajadi, M. Wolf, and T. Kampfrath, Appl. Phys. Lett. **104**, 091118 (2014).